**ATMOSPHERIC AND SURFACE RETRIEVALS IN THE MARS POLAR REGIONS FROM THE THERMAL EMISSION SPECTROMETER MEASUREMENTS.** J. Eluszkiewicz[1], J.-L. Moncet[1], M. W. Shephard[1], K. Cady-Pereira[1], T. Connor[1], and G. Uymin[1], [1]Atmospheric and Environmental Research, Inc., 131 Hartwell Ave., Lexington, MA 02421, jel@aer.com.

**Introduction:** The Thermal Emission Spectrometer (TES) aboard the Mars Global Surveyor (MGS) spacecraft has generated an unprecedented wealth of information about Mars. Although TES is primarily a surface-oriented instrument [1, 2], analyses of TES spectra have also yielded abundant information about the martian atmosphere, including its thermal structure, dust opacity, column abundance of water vapor, and optical properties of airborne dust and water ice particles [3-7]. The information about the spatial and temporal variability in these parameters has in turn enabled a wide range of scientific studies. In particular, TES retrievals have led to a description of the amplitudes, dominant wave periods, and seasonal evolution of planetary waves [8-12], provided insights into dust storm generation mechanisms [13], and, together with the Viking data, have served as a reference to studies of the Mars water cycle [14].

The focus of the TES retrieval and analysis work performed to date has been on the non-polar regions. For example, the opacity product in the Planetary Data System (PDS) is essentially non-existent when the surface temperature drops below about 220 K. This is principally due to the generally small thermal contrast between the atmosphere and the surface, particularly in situations when the surface has near-black-body emissivities [6]. Furthermore, the polar temperature profiles in the PDS have been obtained without specifically accounting for the polar surface emissivities (which are often very different from the non-polar emissivities) and they exhibit little vertical structure (see below).

To some extent, the lack of vertical structure in the TES temperature profiles retrieved to date stems from the coarse vertical resolution of the instrument (10 km or more in the nadir mode). However, the TES temperature profiles in mid-latitudes do exhibit vertical structure and are generally consistent with the MGS radio science (RS) retrievals [15]. This points to other factors playing a role. Indeed, using an independent retrieval algorithm [16], we have performed simultaneous retrievals of atmospheric temperatures and surface emissivity in the polar regions covered by seasonal $CO_2$ frost and established that, even when the coarse vertical resolution of TES is taken into account, the retrieved temperature profiles exhibit inversions around 1 mbar that are present in the newest GCM polar simulations, but largely absent in the PDS profiles. These results are discussed in more detail below.

**Results:** In our TES retrieval work to date [16], we have focused on the polar regions covered with the seasonal $CO_2$ frost, where the presence of both non-porous (slab-like) $CO_2$ ice and more porous, fluffy frost were predicted [17], a prediction confirmed by subsequent analyses [18, 19] (for completeness, we note that dust coating can also mimic the slab-ice behavior [20]). A fluffy texture can be distinguished from a slab layer by the shape of the 25-μm band of solid $CO_2$ [21] seen in the TES spectra, with large band depth $BD_{25}$ indicative of high porosity. $BD_{25}$ is defined as the fractional drop in the measured band radiance relative to the expected blackbody radiance at the brightness temperature of adjacent continua [18]. Sample TES spectra of the southern seasonal cap with small and large $BD_{25}$ are shown in Figure 1.

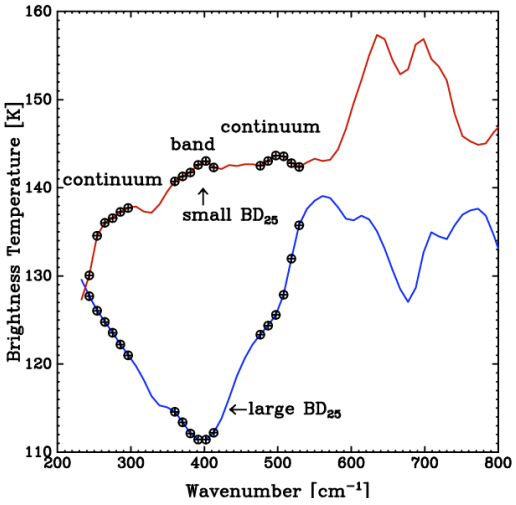


Figure 1: Examples of TES spectra of the southern polar cap. Circles mark spectral locations of channels used to define the 25-μm band (the band itself and two continua). The blue spectrum has low brightness teperatures in the 25-μm band and corresponds to a highly porous deposit. The red spectrum, with a small $BD_{25}$, corresponds to slab ice.

A starting point for our analysis were polar rings corresponding to the northern- and southernmost latitudes of the MGS orbit ($\pm 87°$) that are characterized by almost daily repeat coverage. As discussed in [22], both rings are covered by slab ice (small $BD_{25}$) during prolonged periods in fall and winter, while large values of $BD_{25}$ (i.e., "cold spots") occur sporadically, being more prevalent in the north. The time scale for the disappearance of cold spots is typically short, on the order of several sols (according to [22], this can be explained by metamorphism of freshly-fallen fluffy $CO_2$ snow into slab ice). As a result, atmospheric temperature

retrievals over cold-spot locations must be accompanied by simultaneous retrievals of surface emissivities.

In the pilot study described in [16], we performed retrievals on 148 spectra with low $BD_{25}$ (< 0.05) and 140 spectra with high $BD_{25}$ (> 0.20) included in the northern polar ring data around 87°N during fall and winter analyzed by [22]. The retrieved quantities were atmospheric temperatures, spectrally resolved surface emissivities, and optical depths of atmospheric water ice and dust. For the atmospheric particulates, we ignored scattering, instead using their spectral absorption coefficients available from the PDS [6] and retrieving their optical depth. The impact of neglecting scattering is, in general, not large. For the small dust and ice optical depths we retrieve (see Figure 5 below), the differences between non-scattering radiances and radiances computed using the scattering version of our radiative transfer code are, on average, within the instrument noise level of 0.3 K. For some profiles, the differences do exceed the noise level, and these profiles will be identified in the course of our planned work as part of our quality control procedure. With regard to the surface temperature $T_{skin}$, we essentially set it to the condensation temperature of $CO_2$ frost $T_{frost}$ at the assumed surface pressure. In the retrieval, this is accomplished by assigning $T_{skin}$ to $T_{frost}$ *a priori*, while allowing the retrieved $T_{skin}$ to vary slightly (see Figure 5 below).

Figure 2 shows the atmospheric temperature profiles retrieved for locations characterized by near-unity emissivities (panel *a*) and the so-called "cold spots" where emissivities are significantly lower than unity (panel *b*). Since cold spots are usually attributed to the occurrence of snowfall [23], it is encouraging to see that the associated temperature profiles do fall below the $CO_2$ condensation line (plotted in green in Figure 2) more often than in the low-$BD_{25}$ locations (where the $CO_2$ frost is likely to form directly on the ground). Admittedly, the occurrence of a supersaturated region does not imply snowfall at a given time and location, but we expect that a supersaturated region is associated with snowfall nearby. The super-saturated region in Figure 2 is confined to the lowest 20 km (for an approximate altitude scale, see Figure 3 below), which is consistent with the altitude range of previous detections of $CO_2$ clouds [24, 25].

The shape of our retrieved profiles in Figure 2 exhibits a warming between 1 and 0.1 mbar. While the reality of this shape is somewhat questionable, given the limited number of degrees of freedom and a very coarse vertical resolution above 15 km, the small *a posteriori* errors in this altitude region (shown as dashed red lines in panels *a* and *b* of Figure 2) indicate that the shape does differ from linear. Furthermore, the qualitative aspects of the shape in our temperature profiles around 1 mbar are consistent with the newest GCM runs that take into account interplays between cloud microphysics, convection, and large-scale dynamics [26].

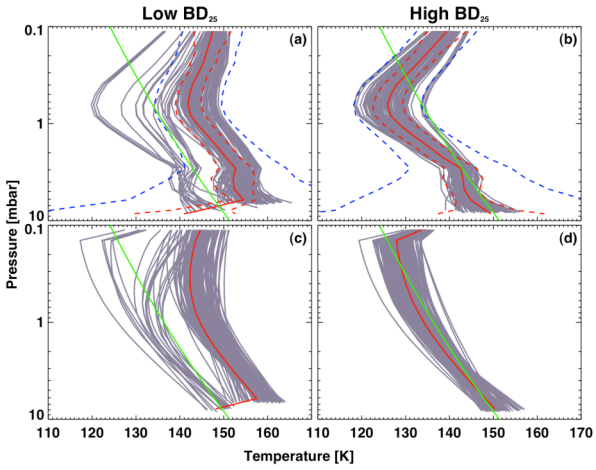


Figure 2: (*a*) and (*b*): Atmospheric temperature profiles retrieved using AER's algorithm for the low and high $BD_{25}$ spectra. (*c*) and (*d*) Their counterparts available from the PDS. The solid red lines represent the mean retrieved profile in each case, while the green lines represent the profile of the $CO_2$ condensation temperature. For our profiles, the dashed blue and red lines represent *a priori* and *a posteriori* error estimates, respectively, around the mean profile (see error analysis in the text).

For comparison, in panels (*c*) and (*d*) of Figure 2 we show the corresponding temperature profiles available from the PDS. The PDS profiles show the same general features as our profiles (colder for high-$BD_{25}$ locations), despite not considering $CO_2$ frost emissivities specifically in their surface treatment. This indicates that this aspect of both retrieval approaches is not overly sensitive to the treatment of surface emissivity. On the other hand, the PDS profiles are significantly more linear above 1 mbar, particularly in the cold-spot locations. It should be emphasized that the profiles shown in Figure 2 have been retrieved using three elements in the empirical orthogonal function (EOF) representation employed in our retrieval algorithm. This limited number of EOFs, consistent with the estimated number of the degrees of freedom (see below), only allows for retrieving the gross features of the true atmospheric profiles. In order to assess the realism of the profiles shown in Figure 2 we plot the *a priori* and *a posteriori* error estimates, corresponding to the diagonal elements of the *a priori* covariance matrix $S_{prior}$ and its *a posteriori* counterpart

$$S_{post} = \left(K^T S_\varepsilon^{-1} K + S_{prior}^{-1}\right)^{-1} \quad (1)$$

where $S_\varepsilon$ is the measurement error matrix, assumed diagonal with diagonal elements equal to the TES nominal noise level (0.3 K), and $K$ is the Jacobian matrix (derivative of channel radiance with respect to the temperature at a given retrieval level). The *a priori* covariance $S_{prior}$ has been derived from a set of GCM profiles. Comparing the magnitude of the *a priori* and *a posteriori* errors in Figure 2 it is clear that there is enough information in the TES radiances to reduce the *a priori* errors significantly. Furthermore, we have computed the averaging kernels to show the sensitivity of the retrievals,

$$A = \left(K^T S_\varepsilon^{-1} K + S_{prior}^{-1}\right)^{-1} K^T S_\varepsilon^{-1} K \qquad (2)$$

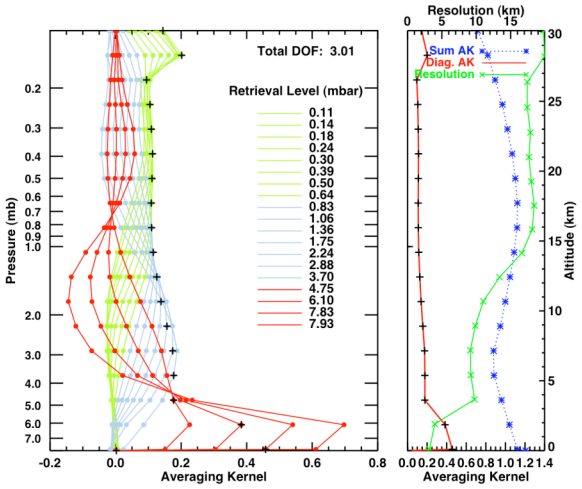


Figure 3: Averaging kernels for the TES retrievals described in the text. The left panel shows the rows of the averaging kernel $A$ for the individual retrieval levels (in mbar, with the surface pressure at 8.13 mbar), while the right panel shows the vertical profiles of the cumulative averaging kernel and its diagonal elements. Shown in green in the right panel is the approximate vertical resolution of the TES temperature retrieval, computed from the full-width-at-half-maximum of the rows of the averaging kernels. The reference altitude scale is shown along the right axis. The total number of degrees of freedom in the retrievals, computed as $Tr(A)$, is equal to 3.

The rows of $A$ are functions of finite width that give a measure of the vertical resolution of the retrieval [27]. They are plotted in Figure 3 and are colored into three distinct altitude groups. The diagonal element of $A$ vanishes at the level closest to the surface (surface pressure is 8.13 mbar for the profile selected for the computation shown in Figure 3), reflecting the lack of information to retrieve the atmospheric temperature at this level. The total number degrees of freedom for signal, which gives the number of independent pieces of information from the measurement, is computed as the trace of $A$. Provided the retrieval is relatively linear, the sum of each row of $A$ represents the fraction of information in the retrieval that comes from the measurement rather than the *a priori*. The amount of available information and the vertical distribution of this information vary, depending on the atmospheric and surface conditions for upwelling radiance observations. The vertical resolution of our retrievals, defined as the half-width at half-maximum of the row of the averaging kernel (approximated as a Gaussian) at each pressure level, is plotted in green in the right panel of Figure 3. The resolution is about 5-10 km in the lowest scale height, but degrades aloft, reaching 20 km at pressures less than 1 mbar. With such coarse resolution, it is only possible to assign the broadest features to the retrieved profiles.

Of particular interest to the interpretation of our results are the retrieved surface emissivities, shown in Figure 4. The *a priori* for surface emissivities is set to a constant value of 0.8 in our retrievals and this value has been adopted after a sensitivity study: with a significantly lower or higher emissivity *a priori*, the retrieved $T_{skin}$ are significantly higher or lower than $T_{frost}$, respectively. As expected, for the cold-spots the retrieved emissivities do deviate significantly from unity in the 25-micron (400 $cm^{-1}$) "transparency band" of solid $CO_2$ and their spectral shape is qualitatively consistent with simulated snow emissivities [22]. In contrast, for the low-$BD_{25}$ spectra, the retrieved emissivities are flat, but significantly less than unity (0.8-0.9), which is not supported by modeling. The cause of these spectrally uniform deviations from blackbody behavior remains to be investigated, but they might be caused by systematic errors not accounted for in our retrieval. Indeed, with a zero-radiance-level correction applied to the TES spectra [1, 18], the retrieved emissivities are brought somewhat closer to unity (by about 0.05-0.1). In the future, we will attempt to remove the remaining deviations by retrieving empirical correction factors necessary to yield blackbody emissivities while constraining $T_{skin}$ to be close to $T_{frost}$ and fitting these factors using the correction software developed by Joshua Bandfield. However, even at the present stage a comparison between the magnitudes of the *a priori* and *a posteriori* errors in Figure 4 reveals that there is enough information in the TES radiances to reduce the *a priori* errors on surface emissivity significantly. Furthermore, the estimated number of degrees of freedom is unity at each emissivity spectral point within the spectral range shown in Figure 4, underscoring the ability of the retrieval to "move away" from the *a priori*. A systematic comparison between the retrieved emissivities and the predictions from the emissivity model described in [22] is planned for the future.

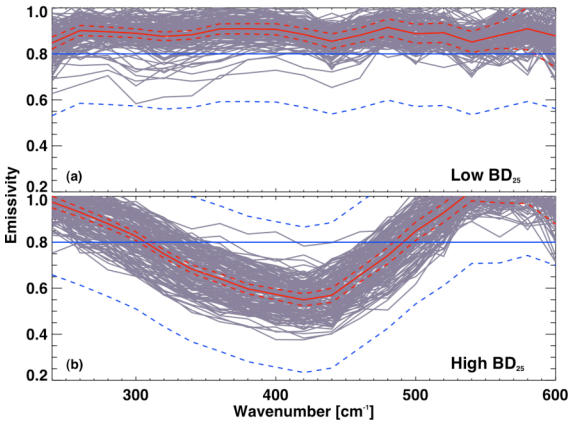


Figure 4: Retrieved surface emissivities. The red solid and dashed lines represent the mean retrieved emissivity and its *a posteriori* errors and the blue solid and dashed lines represent the *a priori* emissivity and its errors.

Figure 5 shows the retrieved surface temperatures and dust opacities (retrieved water ice opacities are very small and are not shown here). As discussed above, the distribution of $T_{skin}$ is centered on $T_{frost}$ by design. The retrieved dust opacities are generally low, consistent with the "flushing" of the wintertime polar atmosphere by precipitating snow, with a hint of slightly lower opacities in the high-$BD_{25}$ case (suggesting more active flushing in the putative snowfall locations). Future research will establish whether these conclusions hold in general (e.g., whether they are sensitive to the assumption of no scattering).

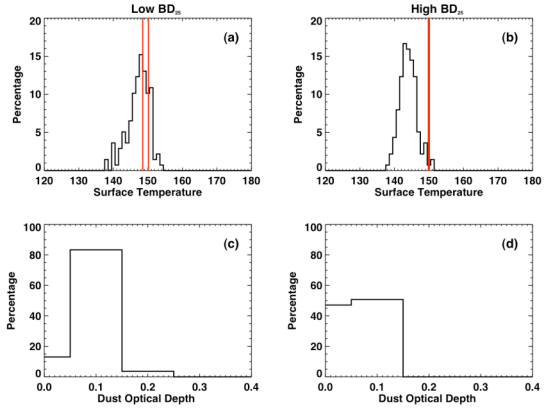


Figure 5: Histogram of the retrieved surface temperatures $T_{skin}$ and dust optical depths. The red lines in panels (*a*) and (*b*) represent the range of $CO_2$ condensation temperatures corresponding to the surface pressures available from the PDS.

**Future Plans:** We plan to extend the pilot study described herein to a larger sample of TES polar measurements. Motivated by our polar results, we will perform retrievals in the tropics as well, with a particular goal of determining whether temperature inversions, present in the RS data [28], but not reported in the PDS TES temperature retrievals, can be retrieved from the TES radiances and if so, whether their magnitude and spatial patterns are consistent with GCM simulations. In addition, the water vapor column retrievals will be updated, incorporating the latest spectroscopic advances [29, 30], and new surface emissivity retrievals will be carried out in situations where the thermal contract between the atmosphere and the surface allows them. Eventually, the new retrievals will be utilized in the Mars Data Assimilation System being developed at the University of Maryland.

**Acknowledgement:** This work has been supported by the NASA Mars Fundamental Research and Mars Data Analysis Programs.

**References:** [1] Christensen P. R. et al. (2001) *J. Geophys. Res., 106,* 23,823. [2] Bandfield J. L. et al. (2000) *Science 287,* 1626. [3] Conrath B. J. et al. (2000) *J. Geophys. Res., 105,* 9,509. [4] Smith M. D. et al. (2000) *J. Geophys. Res., 105,* 9,539. [5] Smith M. D. (2002) *J. Geophys. Res., 107,* 5115. [6] Smith M. D. (2004) *Icarus*, *167,* 148. [7] Wolff M. J. and R. T. Clancy (2003) *J. Geophys. Res., 108,* 5097. [8] Wilson R. J. (2000) *Geophys. Res. Lett., 27,* 3889. [9] Wilson R. J. et al. (2002) *Geophys. Res. Lett.*, *29,* 10.1029/2002GL014866 [10] Banfield D. et al. (2003) *Icarus*, *161,* 319. [11] Banfield D. et al. (2004) *Icarus*, *170,* 365. [12] Wang H. et al. (2005) *J. Geophys. Res., 110,* E07005. [13] Wang H. et al. (2003) *Geophys. Res. Lett., 30,* 1488. [14] Richardson M. I. and R. J. Wilson (2002) *J. Geophys. Res.*, *107,* 10.1029/2001JE001536. [15] Hinson D. P. et al. (2004) *J. Geophys. Res., 109,* E12002, doi:10.1029/2004JE002344. [16] Eluszkiewicz J. et al. (2008) *J. Geophys. Res.,* doi:10.1029/2008JE003120 (in press). [17] Eluszkiewicz J. (1993) *Icarus, 103,* 43. [18] Kieffer H. H. et al. (2000) *J. Geophys. Res., 105,* 9653. [19] Titus T. N. et al. (2001) *J. Geophys. Res., 106,* 23,181. [20] Langevin Y. et al. (2006) *Nature, 442,* 790. [21] Hansen G. B. (1997) *J. Geophys. Res., 102,* 21,569. [22] Eluszkiewicz J. et al. (2005) *Icarus, 174,* 524. [23] Colaprete A. et al. (2005) *Nature, 435,* 184. [24] Pettengil G. H. and P. G. Ford (2000) *Geophys. Res. Lett., 27,* 609. [25] Ivanov A. B. and D. O. Muhleman (2001) *Icarus, 154,* 190. [26] Colaprete A. et al. (2008) *Planet. Space Sci., 56,* 150. [27] Rodgers C. D. (2000) *Inverse Methods for Atmospheric Sounding: Theory and Practice.* World Scientific. [28] Hinson D. P. and R. J. Wilson (2004) *J. Geophys. Res., 109,* E01002 [29] R. Gamache (2008) personal comm. [30] Brown L. R. et al. (2007) *J. Mol. Spectrosc., 246,* 1.